# Journal of Materials Chemistry A

Accepted Manuscript


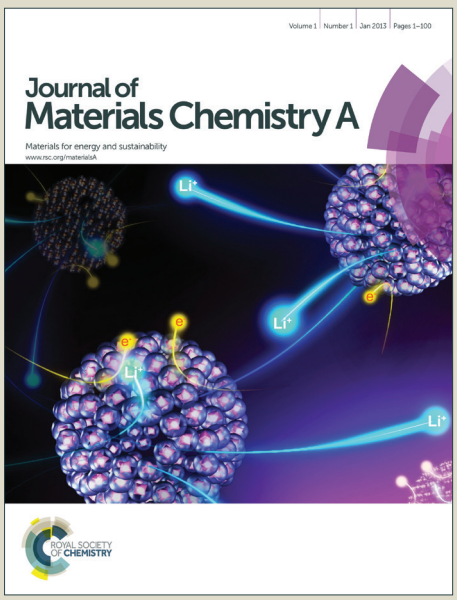





ROYAL SOCIETY OF CHEMISTRY

www.rsc.org/materialsA

# Mo-doped $LiV_3O_8$ nanorod-assembled nanosheets as a high performance cathode material for lithium ion batteries

Huanqiao Song[a, *], Yaguang Liu[a], Cuiping Zhang[a], Chaofeng Liu[a] and Guozhong Cao[a, b, *]

[a]*Beijing Institute of Nanoenergy and Nanosystems, Chinese Academy of Sciences, Beijing 100083, China.*

[b]*Department of Materials and Engineering, University of Washington, Seattle, WA 98195-2120, USA*

**Abstract:**

Mo-doped $LiV_3O_8$ nanorod-assembled nanosheets were prepared by a simple hydrothermal reaction with $LiOH \cdot H_2O$, $V_2O_5$ and $(NH_4)_6Mo_7O_{24}$ as precursors followed with thermal annealing. X-ray diffraction results show that the intensity of the (100) peak is less than that of $(\bar{1}11)$ in Mo-doped $LiV_3O_8$ nanosheets, suggesting the inferior crystallinity of Mo-doped $LiV_3O_8$. The shifts of Raman bands to lower wavenumbers are found in Mo-doped $LiV_3O_8$ material comparing with that in pure $LiV_3O_8$, indicating that $Mo^{6+}$ substitutes $V^{5+}$ in $LiV_3O_8$ layer. X-ray photoelectron spectroscopy reveals that the Mo-doped $LiV_3O_8$ nanosheets calcined at 400℃ contain 25% $V^{4+}$ and 3.5% oxygen vacancies, which likely compensates with the accommodation of 5% $Mo^{6+}$. The Brunauer-Emmett-Teller surface area of Mo-doped $LiV_3O_8$ nanosheets calcined at 400℃ is 24.8 $m^2 g^{-1}$, which is nearly double of $LiV_3O_8$ calcined at 400℃ (13.9 $m^2 g^{-1}$). Electrochemical and lithium ion intercalation properties of both pure and Mo-doped $LiV_3O_8$ cathode are systematically studied by means of cyclic voltammetry, chronopotentiometry, and electrochemical impedance spectroscopy. The Mo-doped $LiV_3O_8$ cathode shows much higher lithium ion storage capacity, better cyclic stability, and higher rate capability than pure $LiV_3O_8$ cathode. The maximum discharge capacity of Mo-doped $LiV_3O_8$ (calcined at 400℃) cathode is 269.0 mAh $g^{-1}$ and retains 205.9 mAh $g^{-1}$ at a current density of 300 mA $g^{-1}$, much

* Corresponding author at: Beijing Institute of Nanoenergy and Nanosystems, Chinese Academy of Sciences, Beijing 100083, China.
E-mail: songhuanqiao@binn.cas.cn; gzcao@u.washington.edu.

higher than 97.8 mAh $g^{-1}$ of $LiV_3O_8$ (also calcined at 400℃) cathode at the $100^{th}$ cycle. Mo-doping is found to increase the electrochemical reaction reversibility, reduce the electrochemical reaction resistance, and enhance the lithium ion diffusivity. The possible reasons for such significant enhancement in discharge/charge capacity, cyclic stability and rate performance of the Mo-doped $LiV_3O_8$ cathode are elucidated based on the structure analysis.

**Keywords:** Mo-doped $LiV_3O_8$ nanosheets; Cathode material for Li-ion batteries; Oxygen vacancy; Electron/Li-ion transport; High capacity and rate capability

## 1. Introduction:

Lithium-ion battery technology has attracted considerable attention due to the dramatically growing demand for safe, efficient, small size and cost effective electrical energy storage systems [1-3]. Lithium-ion batteries (LIBs) have been widely used in portable electronic devices, implantable medical devices, and electric vehicles, however, their performances lag far behind the rapidly increasing demands of ever advancing electronic devices. It is imperative to develop new electrode materials and/or improve existing electrode materials, with higher discharge capacity, cycling stability and rate capability. Compared with anode material, the exploration of cathode material with higher discharge capacity and cycling stability remains a great challenge for the development of next generation LIBs as their energy storage performances are cathode limited [4, 5]. Among cathode materials for LIBs, layered monoclinic lithium trivanadate ($LiV_3O_8$) has gained great interest due to its high specific capacity, low cost, and good safety features [6-8].

$LiV_3O_8$ has excellent suitability as an intercalation host, and is composed of two basic structural units, $VO_6$ octahedra and $VO_5$ distorted trigonal bipyramids, which form two different sites for lithium ions, octahedral and tetrahedral [9]. The $VO_6$ octahedra form a zigzag double ribbon and the $VO_5$ bipyramids form another zigzag ribbon parallel to the $VO_6$ double ribbon. The two ribbons are connected through corner-sharing oxygen ions to form a V-O layer. The V-O layers are held together through the pre-existing lithium ions at octahedral sites [10]. Over three equivalents of lithium ions can intercalate into tetrahedral sites of $LiV_3O_8$ [9]. Almost all the vanadium components exist in pentavalent state in octahedra, and the remaining vanadium components are presented in tetravalent state due to the occupation of the tetrahedral sites by excess lithium ions in discharge process [11]. The theoretical capacity of $LiV_3O_8$ with 3 Li intercalations/deintercalations is about 280 mAh $g^{-1}$, much higher than those of currently used cathode materials [12-14], making it a very promising cathode material for next-generation LIBs. However, $LiV_3O_8$ as a cathode material has relatively low electronic conductivity (approximately $10^{-6}$ S $cm^{-1}$) [15, 16] and low Li-ion diffusion coefficient (*i.e.,* $\sim 10^{-13}$ $cm^2$ $s^{-1}$) [17], both of which

significantly limit its electrochemical property and practical applications as a cathode in LIBs. Numerous strategies have been investigated with the aim at the improved electrical conductivity and diffusion coefficient of $LiV_3O_8$, including synthesis of different structured material, metal ion doping, carbon or other conductive material coating, and reducing particle size to nanometers [8, 18-21]. All of these methods have improved the electrochemical properties, including discharge capacity, rate capacity, and cycle performance, through the reduced transport lengths for both electrons and Li ions, or increased electrode/electrolyte contact area, or easy accommodation of the strain of Li ion insertion/extraction [7, 18, 22-24]. However, the comprehensive performances of $LiV_3O_8$ cathodes need to be further improved for practical applications. For example, Mo *et al.* [8] synthesized $LiV_3O_8$ nanorods on graphene. The reversible capacity is stable at 251 mAh $g^{-1}$ after 10 cycles at a rate of 100 mA $g^{-1}$, but its reversible capacity decreases to 98 mAh $g^{-1}$ when increasing the discharge/charge rate to 1500 mA $g^{-1}$. Hierarchical plate-arrayed $LiV_3O_8$ as cathode material for LIBs present a relatively lower discharge capacity of 226.4 mAh $g^{-1}$ at 1/6 C, but they possess a much higher reversible capacity of 111.8 mAh $g^{-1}$ at 10 C [24].

In this work, we report the synthesis of Mo-doped $LiV_3O_8$ (MDLVO) nanorod-assembled nanosheets electrode by a simple hydrothermal reaction followed with thermal annealing, without any additive. The MDLVO electrodes demonstrated high capacity and excellent rate performance and cycle performance. Various analytical methods, including X-ray diffraction (XRD), thermogravimetric/differential thermal analysis (TGA/DTA), Raman spectrum, scanning electron microscopy (SEM), transmission electron microscopy (TEM), X-ray photoelectron spectroscopy (XPS), were used to investigate the chemical composition, and microstructures and morphologies. Electrochemical and lithium ion intercalation properties of both pure and MDLVO cathodes are systematically studied and the correlations between the excellent electrochemical performance and the microstructure of MDLVO are elucidated.

## 2. Experimental

All the starting materials were of analytically pure grade and used directly without any purification. Mo-doped $LiV_3O_8$ nanorod-assembled nanosheets were prepared by a typical hydrothermal synthesis followed with thermal annealing method as illustrated as Figure 1. In the typical synthesis, $(NH_4)_6Mo_7O_{24}$, $V_2O_5$ and $LiOH^{\cdot}H_2O$ were dissolved in distilled water in sequence under room temperature with constant stirring. The molar ratio of Li: V: Mo was kept at 1.05: 2.85: 0.15 in the solution. And then the mixture was heated at 80℃ for several hours with vigorous stirring to evaporate the water (2/5 was removed) until a yellow-brown sol was generated. The sol, exhibiting a PH of ~4, was then transferred into a 100 ml Teflon lined stainless steel autoclave. The autoclave was heated at 180℃ for 48 h and then cooled to room temperature quickly. The MDLVO gel was freeze-dried in order to prevent agglomeration, and further treated at different temperatures (300, 350, 400 and 450℃) for 2 h in air. The samples were then milled to obtain MDLVO nanorod-assembled nanosheets, and they were designated MDLVO (300), MDLVO (350), MDLVO (400) and MDLVO (450) according to the calcination temperatures, respectively. For comparison, $LiV_3O_8$ without Mo was also prepared using the same method and calcined at 400℃ for 2 h.

XRD was performed on a Bruker powder diffraction system (model D8 Advanced) with a Cu-Kα radiation source. The 2θ angular regions between 10° and 70° were investigated at a scan rate of 6° $min^{-1}$ with a step of 0.02°. Raman spectra were collected at ±0.65 $cm^{-1}$ resolution with a Horiba JOBIN YVON Raman system (LabRAM HR Evolution) using an argon ion laser (532 nm) as the excitation source. XPS analysis was conducted on a K-Alpha 1063 instrument using monochromatic Al Kα X-ray source operated at 72 W. Charging effects were corrected by adjusting the binding energy of C 1s to 284.6 eV in the XPS spectra. A non-linear, least-squares algorithm was employed to determine the best fit to each of the V 2P core level spectra with two Gaussian-Lorentzian curves corresponding to two oxidation states ($V^{4+}$ and $V^{5+}$). The relative atomic ratio of $V^{4+}$ and $V^{5+}$ was determined from the

respective area ratios of these fits. The elemental composition of MDLVO nanosheets was determined using an energy dispersive X-ray spectrometer (OXFORD INCA 300).

The morphology and energy dispersive spectroscopy (EDS) mappings of the as-prepared composite materials were detected by field emission scanning electron microscope (FE-SEM, SU 8020) at 10 kV. TEM investigations were performed using a JEOL JEM-2010 instrument with an accelerating voltage of 200 kV. $N_2$ adsorption–desorption analysis was carried out using a Micromeritics ASAP 2020 HD88. The typical sample weight used was about 500 mg. The outgas condition was set to 240 min at 250℃ under vacuum, and all adsorption–desorption measurements were carried out at liquid nitrogen temperature. A combined TGA/DTA instrument (Mettler-Toledo STAR system, TGA/SDTA) was used to study the decomposition and reaction of the precursors

The working electrode was prepared by mixing the active material, polyvinylidene fluoride, and Super P conductive carbon in the weight ratio of 70: 10: 20. N-methylpyrrolidone was used as the solvent. The resultant slurry was then uniformly cast onto Al foil current collector and dried overnight at 80℃. After solvent evaporation and heating at 120℃ under vacuum for 12 h, the electrodes were cut into disks and assembled into CR2025 coin type cells in a glove box filled with pure argon gas. A Celgrade polypropylene was used as separator. The electrolyte was 1 M $LiPF_6$ in a mixture of ethylene carbonate and dimethyl carbonate (1:1). Li metal was used as the counter electrode and reference electrode. The mass density of the active material in each electrode disk is 2.5-3.5 mg $cm^{-2}$. The electrochemical performances of the prepared electrodes were characterized with a Land CT2001A tester system at room temperature. The cells were galvanostatically discharged and charged at different current density within the range of 2.0-4.0 V (*vs*. $Li/Li^+$). Cyclic voltammetry (CV) tests were carried out using Solartron electrochemical workstation with a scan rate of 0.1 mV $s^{-1}$ at room temperature. The specific capacity and the current density were calculated based on the mass of active material. Electrochemical impedance spectroscopy (EIS) experiments were performed using the Solartron 1287A in

conjunction with a Solartron 1260A impedance analyzer over the frequency range from 100 kHz to 0.01 Hz and the AC amplitude was 10.0 mV. Before the EIS test, the cells were charged to 2.7 V and then kept at that voltage for a period of time to reach a stable state. The electrical conductivities of the prepared samples were measured by the direct current (DC) four-probe technique, as described elsewhere [25, 26]. The sample was made into a pellet at a pressure of 100 MPa, and then the pellet was gold coated, dried and sandwiched between stainless steel blocking electrodes for electrical conductivity measurements.

## 3. Results and discussion

Figure 2 shows the TGA-DTA results of the MDLVO cryogel under flowing air with a ramping rate of 5℃ $min^{-1}$. In the temperature range between 28 and 165℃, the gradual weight loss of 9.4% is assigned to the evaporation and removal of $NH_3$ or water bonded physically to MDLVO cryogel, corresponding with an obvious endothermic peak in the DTA curve. The subsequent weight loss of 3.2% between 165 and 325℃ can be ascribed to the deintercalation of chemically bonded water and the formation of crystalline MDLVO. No appreciable weight loss in TGA at temperatures above 325℃ was found, which suggests that the removal of chemically bonded water has completed at 325℃. There is a big and wide exothermic peak in the range of 420-530℃ on the DTA curve but the weight of the sample keeps constant, which is likely due to the further crystallization of MDLVO [27].

The XRD patterns for $LiV_3O_8$ and the as-prepared MDLVO nanosheets heat-treated at different temperatures (300℃, 350℃, 400℃ and 450℃) are shown in Figure 3. It can be seen that the MDLVO samples calcined at temperatures between 300 and 450℃ exhibited almost identical XRD patterns, which could be readily indexed into a monoclinic crystalline $LiV_3O_8$ phase (JCPDS Card No. 72-1193, space group: $P2_1/m$), though the diffraction peak intensity (in curves b-e) changes with the temperatures. The diffraction peaks of MDLVO become sharp and narrow when the calcination temperature increased from 300 to 450℃, implying that the primary particle grew up with the temperature increase. The average crystallite sizes were calculated from $LiV_3O_8$ (312) peak by Scherrer Formula and they are 9.70 nm for MDLVO (300),

14.31 nm for MDLVO (350), 19.72 nm for MDLVO (400) and 23.96 nm for MDLVO (450), respectively. Comparing the patterns of MDLVO with that of pure $LiV_3O_8$, no crystalline molybdenum or molybdenum oxides were observed in MDLVO patterns. A small impurity phase of $Li_{0.3}V_2O_5$ was detected at ~12.3° in pure $LiV_3O_8$ pattern, but not found in MDLVO patterns. Moreover, it is noted that the intensity of the (100) peak is less than that of $(\bar{1}11)$ in MDLVO, which is different from the $LiV_3O_8$ in this work and in literature [28-30]. Wang *et al.* [20] have ascribed the low intensity of the (100) peak to inferior crystallinity. Except these, the peak position and the peak intensities of the pure and doped $LiV_3O_8$ are similar, which suggests that ion doping does not change the lattice parameter obviously. The Raman spectrum is more sensitive to the doping sites and is considered a more suitable method to investigate the doping ions in the $LiV_3O_8$ crystal lattice. Therefore, we measured the Raman spectra of the pure and doped $LiV_3O_8$ calcined at 400℃, and the results are shown in Figure 4. The Raman band of pure $LiV_3O_8$ at 994 $cm^{-1}$ is attributed to the vibrational modes belonging to the $A_g$ symmetry, and can be assigned to V-O stretching vibrations of the $VO_5$ pyramids [31], and the band at 771 $cm^{-1}$ is probably due to the atomic motions of corner-sharing oxygen among the $VO_6$, $VO_5$, and $LiO_6$ polyhedron [31, 32]. The symmetry stretching modes in MDLVO shift to lower wave numbers (990 $cm^{-1}$ and 760 $cm^{-1}$) because the mass of $Mo^{6+}$ (95.94) is greater than that of $V^{5+}$ (50.94). The mode shifts mean a little distortion of the crystal cells, which suggests that $Mo^{6+}$ substitutes $V^{5+}$ in the $VO_6$ octahedra and $VO_5$ trigonal bipyramids [33]. In addition, it is apparent that the peak strengths at 990 and 760 $cm^{-1}$ for Mo-doped sample are quite weak compared to that for pure $LiV_3O_8$, this indicates that the short-range local condition is less ordered and less crystallized in Mo-doped sample [31, 34], which is consistent with the XRD results.

The XPS spectra give the information about the surface composition and the valence states of the elements. Figure 5a is the XPS spectrum of MDLVO calcined at 400℃, in which peaks of Li 1s, V 2p, Mo 3d and O 1s are clearly observed. Figure 5b and c are the high resolution XPS of Mo 3d and V 2p after fitting. The peaks at 233.09 and 236.18 eV in Figure 5b correspond to Mo 3d5/2 and Mo 3d3/2, respectively, which

agree well with the literature values for $Mo^{6+}$ in molybdenum oxide or other molybdate [35, 36]. The V 2p spectrum in Figure 5c shows two main peaks at 517.33 and 524.82 eV, which are ascribed to the spin-orbit splitting of the components, $V^{5+}$ 2p3/2 and $V^{5+}$ 2p1/2 [37]. It is noteworthy that the peaks of $V^{4+}$ are also clearly found at 516.23 eV ($V^{4+}$ 2p3/2) and 521.88 eV ($V^{4+}$ 2p1/2) [21], suggesting the formation of low valence state vanadium in MDLVO nanosheets. The relative atomic ratio of $V^{5+}$ and $V^{4+}$ is calculated based on the peak areas, and the result is 3:1, which means that the content of $V^{4+}$ is greatly more than the content of $Mo^{6+}$. In order to compensate the charge, a lot of oxygen vacancies must be created in the lattice of MDLVO. It can be determined that the formula of MDLVO is $LiMo_{0.15}V_{2.85}O_{7.72}(V_O^{\cdot\cdot})_{0.28}$, which is consistent with the results of elemental composition analysis by EDS measurements. The presence of oxygen vacancies leaves more open void space for easy lithium ion diffusion. In addition, the oxygen vacancies may serve as possible nucleation centers for easy phase transformation during the lithium ion insertion and extraction processes [38, 39]. Moreover, the presence of $V^{4+}$ and associated oxygen vacancies can improve the electrical conductivity of cathode [40, 41]. The electrical conductivities of pure $LiV_3O_8$ and MDLVO (400) measured by the DC four-probe technique are $3.52\times 10^{-6}$ S $cm^{-1}$ and $2.89\times 10^{-5}$ S $cm^{-1}$, respectively.

The morphology and structure of MDLVO prepared at 400℃ were characterized by FE-SEM and TEM. As shown in Figure 6a, the nanosheets with the average length of 800 nm~1.5 μm and the width of 1 μm can be observed from the SEM image. Also, it can be found from the close examination in Figure 6b that the MDLVO (400) nanosheets consist of numerous nanobelts 100~200 nm long and of 40~60 nm wide (see Figure 6c and d). The composition of MDLVO (400) can be unraveled by element mapping images of lithium, molybdenum, vanadium and oxygen. It can be seen from Figure 6e that the lithium, molybdenum, vanadium and oxygen distributions are quite uniform; molybdenum is also well distributed over all the $LiV_3O_8$, further suggesting the entry of molybdenum into the lattice of $LiV_3O_8$. FE-SEM analyses of the MDLVO cryogel and the products performed at different temperatures help us to understand how the nanorod-assembled nanosheets form.

Figure S3a and b show the image of MDLVO cryogel. As shown, the cryogel is composed of sheet MDLVO assembled by the ribbon-like MDLVO fiber. This structure is similar with the $V_2O_5$ cryogel or xerogel in literature [42, 43]. In general, $V_2O_5$ cryogel or xerogel is considered to be the long-range order and the local structural disorder [44], the XRD result in Figure S4 presents that the diffraction peaks of MDLVO cryogel were not sharp, which means that the structure of MDLVO cryogel is disordered (or amorphous). The cryogel here is developed from the commercially available $V_2O_5$, LiOH and $(NH_4)_6Mo_7O_{24}$ utilizing additive-free solution processing methods as governed by the following reaction in stainless steel autoclave:

$$28LiOH + 39.9V_2O_5 + 0.6(NH_4)_6Mo_7O_{24} \xrightarrow{180^{\circ}C} 28LiMo_{0.15}V_{2.85}O_8 + 15.8H_2O + 3.6NH_3\uparrow + 1.05O_2\uparrow$$

During the hydrothermal reaction, the ribbon-like MDLVO fibers are formed in gel. The ribbon-like MDLVO fibers intertwine into sheet MDLVO during drying. The MDLVO cryogel is composed of long nanobelts which are about 100 nm wide. The morphology of these nanobelts could be related to the formation of hydrous MDLVO as hydrous $V_2O_5$ did in literature [43-45]. Similar nanobelts were also observed in $Li_{1.2}V_3O_8$ gel by Xie *et al.* [46]. $V_2O_5$ gel provides a kind of matrix for $LiV_3O_8$ gel and therefore $LiV_3O_8$ or MDLVO gel shows a network structure resembling that of $V_2O_5$ gel [46]. The as-prepared samples after calcined show high thermal stability with good retention of the MDLVO sheet structure, which is confirmed by the results of FE-SEM in Figure S3c and d. In addition, it can also be seen that some nanorods grew up from the connection parts of MDLVO nanobelts in Figure S3d, indicating that the disordered structure of MDLVO cryogel has transformed into the ordered structure of nanorods. The nanorod-assembled nanosheets were obtained after ball milling, which have explained the formation mechanism of the nanorod-assembled nanosheets and that the nanorods grew from the nanosheets with the increase of calcination temperature (see Figure S3e-h). Such a nanoscale subunit-assembled nanosheet hierarchical structure (MDLVO (400)) gives rise to a Brunauer-Emmett-Teller (BET) surface area of 24.8 $m^2 g^{-1}$ (shown in Figure 7), which is relatively higher than that of $LiV_3O_8$ (13.9 $m^2 g^{-1}$) and previous reports [6], [28]. The bigger surface area of

MDLVO (400) is favorable for fast electrolyte penetration and lithium ion diffusion. The Barrett-Joyner-Halenda (BJH) desorption analyses indicate that the sample contains mesopores with a size peak of 22.4 nm. These appropriate size mesopores can provide excellent channels and cavities for complete, homogeneous and easy $Li^+$ intercalation and diffusion in the material.

Figure 8 shows the second-cycle CV curves for MDLVO (400) and $LiV_3O_8$ (calcined at 400℃) electrodes at a scan rate of 0.1 mV $s^{-1}$ over the range of 2.0-4.0 V (*vs.* $Li/Li^+$). During the cathodic scan of sample $LiV_3O_8$, the peak at ~3.57 V corresponds to the initial Li ion insertion into the octahedral site of $LiV_3O_8$ host structure [17, 32] and the peak at ~2.72 V belongs to the Li ion insertion in the empty tetrahedral site through a single-phase reaction between $0<x<2.0$ in $Li_{1+x}V_3O_8$, and the peak at ~2.39 V is related to Li ion occupation in tetrahedral sites accompanying with a two-phase transition from $Li_3V_3O_8$ to $Li_4V_3O_8$ ($2.0<x<3.0$) [47-49]. The corresponding anodic peaks for $LiV_3O_8$ at ~3.65 V, ~3.03 V and ~2.55 V are the Li ion extraction reactions. Besides these peaks, one obvious peak at 3.46 V is observed in the anodic san. While two peaks at 3.17 and 3.37 V appear in the cathodic scan. These peaks can be ascribed to the active phase of $Li_{0.3}V_2O_5$ as observed in the XRD result of $LiV_3O_8$, suggesting the different lithium sites with energy difference for lithium ion holding [7, 50, 51]. For MDLVO (400) electrode, the main cathodic peaks shift to ~3.44 V, ~2.76 V and ~2.47 V (as above mentioned, ~3.57 V, ~2.72 V and ~2.39 V for pure $LiV_3O_8$ electrode), and the main anodic peaks shift to ~3.55 V, ~2.84 V and ~2.47 V from ~3.65 V, ~3.03 V and ~2.55 V of $LiV_3O_8$ electrode. The smaller potential intervals of MDLVO (400) electrodes between the cathodic and anodic peaks indicate an excellent reversible insertion/extraction reaction of Li ion. The accommodation of $Mo^{6+}$ stabilizes the $LiV_3O_8$ layer therefore benefits the insertion/extraction process of Li ions within the layered $LiV_3O_8$ structure. Similar results have also been reported for the Ce-doped $LiV_3O_8$ and Si-doped $LiV_3O_8$ [52, 53]. In addition, Su *et al.* [54] ascribed the decrease of potential intervals of the oxidation and reduction peaks to the improvement of electronic conductivity after the formation of carbon coating on $Li_3V_2(PO_4)_3$. For our MDLVO (400) electrode, the

presence of mixed-valence $V^{4+}/V^{5+}$ increased the electrical conductivity of cathode materials [40], thus decreased the polarization of Li ion insertion/extraction reaction. Besides, the cathodic peak at ~2.15 V, which is nearly invisible in the CV curve of $LiV_3O_8$, is attributed to the slower kinetic insertion process of Li ion where the single-phase transition corresponding to the $Li_4V_3O_8$ takes place ($3.0<x<3.2$) [55]. As can be seen in the CV curves for the two electrodes, a higher current intensity on $LiV_3O_8$ electrode at the cathodic peak of 3.57 V was found and a similar current density with MDLVO electrode at 2.72 V was detected on $LiV_3O_8$ electrode. It is believed that the Li ion diffusion efficiency is high in pure $LiV_3O_8$ for the initial insertion. A lot of diffusion paths and empty tetrahedral sites are available for Li ion occupation between layers in the earlier stage of Li ion insertion. Therefore, the Li ion insertion can proceed efficiently in pure $LiV_3O_8$. Pan *et al*. [22] observed the similar phenomenon for the higher current density in bulk $LiV_3O_8$ than that in the nanorod-like $LiV_3O_8$ at the early stage of Li ion insertion. However, the peak current density of pure $LiV_3O_8$ electrode is much lower than that of MDLVO (400) electrode for the two-phase transition at 2.39 V. Kawakita *et al*. [49] reported that the Li ion diffusion coefficient in $LiV_3O_8$ electrode is much lower for the two-phase transition stage and considered that the insertion becomes kinetics limited at this stage. While for the electrode containing $Mo^{6+}$, the BET surface area of the material is almost twice that of pure $LiV_3O_8$, so the required Li ion diffusion distance is effectively shortened. Furthermore, the low crystallinity, quantities of oxygen vacancies and the appropriate pore size distribution can allow easy accommodation of more Li ions during the insertion process, thus lowering the energy barrier for the diffusion process. This also explains the higher current density on MDLVO (400) electrode at 2.15 V during the cathodic scan. During the anodic scan, similar behavior is observed. All of these differences in CV curves confirm the improvement of Li ion insertion/extraction kinetics in MDLVO (400) cathode.

Figure 9 shows the discharge/charge curves and cyclic performance of the pure $LiV_3O_8$ calcined at 400℃ and MDLVO (400) at a current density of 300 mA $g^{-1}$. As can be seen in Figure 9a, a rapid voltage decrease during discharge and a quick

voltage increase during charge were observed in the voltage range between 4 V and 2.8 V for pure $LiV_3O_8$ electrode, followed by three short plateaus from 2.8 V to 2 V, which indicate the multistep processes, and a negligible capacity was obtained in this voltage range. The overall specific discharge capacity was only 105.0 mAh $g^{-1}$. However, as can be seen in Figure 9a, the MDLVO (400) nanorod-assembled nanosheet electrode had more obvious plateaus and higher specific discharge capacity. When the discharge capacities were more stable, it delivered a specific capacity of 218.2 mAh $g^{-1}$ at the 81$^{th}$ cycle, which is almost twice the capacity of the pure $LiV_3O_8$ electrode. Jouanneau *et al.* [56] reported that the particle size and shape greatly influence the insertion rate of Li ion for crystalline $Li_{1+x}V_3O_8$, and the crystal shape (well-formed crystal or no crystal shape) plays a major role on the cyclability. In our case, the uniform MDLVO (400) nanorod-assembled nanosheets with appropriate crystallinity have larger BET surface area and better mesopore space between the particles (shown in Figure 7). This MDLVO cathode exhibits both better utilization of the active material and higher capacity than pure $LiV_3O_8$. Figure 9b shows the cyclic performance of the pure $LiV_3O_8$ and MDLVO (400) electrode. The pure $LiV_3O_8$ electrode delivered an initial specific discharge capacity of 275.0 mAh $g^{-1}$, and its capacity reached 292.0 mAh $g^{-1}$ during the second cycle, however, it sharply decreased to 192.1 mAh $g^{-1}$ at the 20$^{th}$ cycle and further to 97.8 mAh $g^{-1}$ at the 100$^{th}$ cycle. Such a result is in a good agreement with the literature [34, 57, 58], which widely reported a quick capacity loss in initial cycles for pure $LiV_3O_8$. Wang *et al.* [59] reported the $Li_{1.5}V_3O_8$ nanosheets with an initial capacity of 204 mAh $g^{-1}$ at a current density of 175 mA $g^{-1}$, but it decreased to 100 mAh $g^{-1}$ after 100 cycles. Guo *et al.* [60] reported the $LiV_3O_8$ with an initial capacity of 248.5 mAh $g^{-1}$ at 300 mA $g^{-1}$. However, the capacity faded to 105.2 mAh $g^{-1}$ rapidly during the first 50 cycles. The capacity fading may result from the irreversible phase transition between $LiV_3O_8$ and $Li_4V_3O_8$ [61], or deterioration of crystal structure and the dissolution of small amount of $V^{III}$ in the electrolyte [62]. For our MDLVO (400) electrode, the specific capacity and cycle stability were significantly enhanced, although it delivered a initial discharge capacity of 217.1 mAh $g^{-1}$ at the current density of 300 mA $g^{-1}$. The discharge

capacity steadily increased to 269.0 mAh $g^{-1}$ at the 13$^{th}$ cycle, which is equivalent to 2.9 mol Li per mol of $LiV_3O_8$. Then the specific discharge capacity slightly decreased to 230.2 mAh $g^{-1}$ at the 49$^{th}$ cycle and became quite stable in subsequent cycles (only 0.47% and 0.25% capacity fading per cycle between cycles 49 and 100 and cycles 49 and 150, respectively). Feng *et al.* [21] found that B doped $LiV_3O_8$ had higher discharge capacity and stability than pure $LiV_3O_8$. They ascribed the good performance to the broader pathway between adjacent vanadate chains for the diffusion of lithium in the material and the more stable layer structure after B doping. Ren *et al.* [19] improved the electrochemical performance of $LiV_3O_8$ by Zr doping. They considered that the Zr substitution for V in $LiV_3O_8$ increased the interlayer spacing of the bulk material and made it more stable during discharge/charge cyclings. In the present study, the substitutional doping of $Mo^{6+}$ also increased the interlayer spacing of $LiV_3O_8$ and stabilized its structure, which leads to the decrease of the irreversible phase transition between $LiV_3O_8$ and $Li_4V_3O_8$ during discharge/charge processes. Besides, the slower activation process of MDLVO (400) nanorod-assembled nanosheet electrode than the pure $LiV_3O_8$ electrode is very similar to the previous report on $V_2O_5$ xerogel electrode [63]. For example, the $N_2$-annealed $V_2O_5$ xerogel electrode presented a low initial discharge capacity of 68 mAh $g^{-1}$, but it increased to 158 mAh $g^{-1}$ at the 24$^{th}$ cycle, which was ascribed to the surface defect layer on the $N_2$-annealed $V_2O_5$ xerogel. In contrast, the air-annealed $V_2O_5$ xerogel electrode started with a high discharge capacity of 152 mAh $g^{-1}$, but the capacity decreased sharply in later cycles and the discharge capacity was only 44 mAh $g^{-1}$ at the 50$^{th}$ cycle. The introduced surface and bulk defects by doping result in a much slower activation and more stable cyclic performance for MDLVO (400) electrode. Therefore, the MDLVO (400) electrode demonstrates a high reversibility for Li ion insertion/extraction reaction and a stable discharge/charge performance. MDLVO (400) electrode retained a high specific discharge capacity of 205.9 mAh $g^{-1}$ even after 100 cycles, which is still twice the capacity of the pure $LiV_3O_8$ electrode.

In order to better understand the electrochemical performance of the MDLVO (400) electrode, the cycle performances at increasing current densities from 100 mA $g^{-1}$ to

1500 mA $g^{-1}$ were determined and shown in Figure 10. For comparison, the testing results of $LiV_3O_8$ (calcined at 400℃) electrode are also listed in Figure 10. As shown in Figure 10a, the discharge capacity of MDLVO (400) electrode measured in the voltage from 4.0 V to 2.0 V was 331.3 mAh $g^{-1}$ at the current density of 100 mA $g^{-1}$ and remained at 124.5 mAh $g^{-1}$ even at the current density of 1500 mA $g^{-1}$. This rate capability is much higher than that of $LiV_3O_8$ electrode, being 200.1 mAh $g^{-1}$ at 100 mA $g^{-1}$ and 82.6 mAh $g^{-1}$ at 1500 mA $g^{-1}$, respectively. The capacities were fairly stable at each current density for the MDLVO (400) electrode even the cell experienced more than 60 cycles at various high current densities. A capacity of 304.8 mAh $g^{-1}$ was obtained when the current density returned to 100 mA $g^{-1}$, which corresponds to 3.27 mol Li per mol of MDLVO (400). Figure 10b presents the discharge/charge curves of MDLVO (400) at various current densities. With the increase of current density, the decreases of discharge plateaus and the increases of charge plateaus were observed, which is attributed to the increasing polarization effect. The capacity and stability could return the initial value after discharge and charge at high current density, indicating the high reversibility of Li ion insertion/extraction. Gao *et al.* [64] considered that Mo doping is an effective way to improve the structural stability and rate performance of $Li_2MnO_3$ cathode materials through improving electron/Li-ion transport and oxygen stability. In our sample, $V^{4+}$ and oxygen vacancies appeared in $LiV_3O_8$ due to the $Mo^{6+}$ doping, which are helpful for improving the electron/Li-ion transport, and the appropriate crystallinity and lattice distortion were found in MDLVO structure, which are favorable to increasing the discharge/charge capacity and structural stability of $LiV_3O_8$. Thus MDLVO (400) electrode presents higher rate performance and better stability than $LiV_3O_8$ electrode. The influence of Mo doping on the rate capabilities is further verified by the comparison of EIS results of activated MDLVO (400) with $LiV_3O_8$ electrodes. Figure 11a shows the Nyquist plots of MDLVO (400) and $LiV_3O_8$ electrodes. The Nyquist plots exhibit two semicircles in the high frequency and medium frequency region. The high frequency semicircle is always related to the interface parameters such as surface film contribution, porous nature of electrode, and/or the bulk of materials. The

mediate semicircle is attributed to the charge-transfer resistance ($R_{ct}$) [65], [66]. And the slope line represents the Warburg impedance ($Z_W$) at the low frequency, meaning the diffusion of Li ions in the solid matrix. Fitting the curves with the equivalent electrical circuit model, where the symbols, $R_s$, $R_f$, $R_{ct}$ and $Z_w$, denote the solution resistance, contact resistance, charge-transfer resistance and Warburg impedance, respectively. The fitting results of $R_s$, $R_f$, and $R_{ct}$ of $LiV_3O_8$ and MDLVO (400) electrodes are shown in Table S1. It can be seen that the $R_f$ and $R_{ct}$ values of MDLVO (400) electrode are 59.6 Ω and 68.1 Ω, respectively, which are smaller than those of pure $LiV_3O_8$ electrode (134.2 Ω and 155.2 Ω), suggesting that the doping of Mo significantly suppresses the rise of both of the surface film resistance and charge transfer resistance. It is clear evidence that the MDLVO (400) electrode possesses the higher electrical conductivity and the faster charge-transfer reaction for lithium ion insertion and extraction than the pure $LiV_3O_8$ electrode, further confirming the high efficient doping of Mo into $LiV_3O_8$. Li ion diffusion coefficient could be calculated from the low frequency plots based on the following Eqs. (1) and (2).

$$Z' = R_e + R_{ct} + \sigma_w \omega^{-1/2} \quad (1)$$

$$D_{Li^+} = \frac{R^2T^2}{2A^2n^4F^4C^2\sigma_W^2} \quad (2)$$

In equation (1), $\omega(2\pi f)$ is the angular frequency in low frequency region, and both $R_e$ and $R_{ct}$ are kinetics parameters independent of frequency, which can obtained from the fitting results of Nyquist plots in Figure 11a. Then the Warburg coefficient ($\sigma_w$) can be obtained from the slope of the fitting line while $Z'$ has a linear relationship with $\omega^{-1/2}$. In equation (2), R is the gas constant, T is the temperature, A is the area of the electrode, n is the number of electron transfer per mole active material involved in the electrode reaction, F is Faraday's constant, and C is the molar concentration of Li ions. Base on the fitting linear equation in Figure 11b, the Li ion diffusion coefficients of $LiV_3O_8$ and MDLVO (400) could be calculated and the results were $2.37\times 10^{-13}$ $cm^2$ $s^{-1}$ and $5.74\times 10^{-12}$ $cm^2$ $s^{-1}$, respectively. The lower surface film and charge transfer resistance and higher Li ion diffusion coefficient and electrical conductivity of MDLVO electrode bring about its superior

rate capabilities and other electrochemical properties.

Figure 12 shows the cyclic stabilities of MDLVO electrodes calcined at different temperatures at a current density of 300 mA $g^{-1}$. The initial discharge capacities of MDLVO electrodes calcined at 300, 350, 400 and 450℃ were 254.7, 226.0, 217.1 and 195.8 mAh $g^{-1}$, respectively. The samples calcined at 300 and 350℃ reached their maximum discharge capacities of 303.1 and 284.6 mAh $g^{-1}$ at the $8^{th}$ cycle, showing a higher initial storage capacity and a quicker capacity increase in the samples calcined at lower temperatures, and then declined monotonically to respective 123.0 and 141.9 mAh $g^{-1}$ at the $100^{th}$ cycle. This poor cycling stability can be attributable to the inferior crystallinity and its unstable structure [56], even though inferior crystallinity could accommodate more lithium ions at their initial stage [62, 67]. The cyclic stability was seen to improve in general, as the calcination temperature increased. However, the discharge capacity of MDLVO (400) electrode was higher than that of MDLVO (450) electrode at all the 100 cycles. MDLVO (400) electrode reached its maximum capacity of 269.0 mAh $g^{-1}$ at the $13^{th}$ cycle, which is much higher than that of MDLVO (450) electrode (198.7 mAh $g^{-1}$ at the $3^{rd}$ cycle) and those reported in literature [1], [27]. The specific discharge capacity of MDLVO (400) electrode was found to retain 205.9 mAh $g^{-1}$ after 100 cycles (a capacity fading rate of only 0.05% per cycle for the initial 100 cycles), while the discharge capacity of MDLVO (450) electrode retained only 163.3 mAh $g^{-1}$ at the $100^{th}$ cycle (the capacity fading rate is 0.17% per cycle for the 100 cycles). The excellent capacity and cyclic stability of MDLVO (400) electrode are likely resulted from the particle size and the aggregation. It can be seen that in Figure 6 and Figure S3, the nanorods and the nanosheets were separate well in MDLVO (400), and this structure allowed good accessibility of electrolyte to active material. While in MDLVO (450) the merge and grown nanorods led to a decrease in the void space available for electrolyte diffusion, which agrees well with the decrease of BET surface area from MDLVO (400) (24.8 $m^2$ $g^{-1}$) to MDLVO (450) (16.9 $m^2$ $g^{-1}$) in Table S2. Therefore, the Mo-doped sample calcined at 400℃ possesses the best electrochemical performance.

The nanosized material is believed to be favorable with shortened Li ion diffusion

distance and more active sites for electrochemical reactions. Recent work showed that the capacity has been enhanced by improving the transport properties of nanostructured $LiV_3O_8$ [22, 27, 68]. However, the poor rate capability is still a problem [22]. The present MDLVO material exhibits not only a very high capacity and good cycling stability, but also an excellent rate performance. A comparison of the electrochemical performance of our MDLVO with some representative reported $LiV_3O_8$ electrode materials is given in Table S3. The outstanding electrochemical performance of MDLVO can be attributed to its higher electrochemical reversibility, higher lithium ion diffusion coefficients and lower electrochemical reaction resistance. Based on the structure analysis, the occupancy of $Mo^{6+}$ could lead to more stable structure. Jouanneau *et al.* [61, 62] have reported that the lattice parameter of $LiV_3O_8$ changes greatly after lithiation during charge and discharge cycles. A contraction of *a* lattice parameter and an expansion of *b* and *c* lattice parameter appear from $LiV_3O_8$ to $Li_4V_3O_8$ at 2.6 V. Thus the capacity fading occurs due to the damage of the crystal structure caused by the abrupt change in cell-lattice constant. The substitutional doping of $Mo^{6+}$ into $LiV_3O_8$ decreases this structural change and improves the electrochemical cycle reversibility. The MDLVO with nanorod-assembled sheet structure has bigger BET surface area than pure $LiV_3O_8$. It has been known that limitation factor for rate capability is the delivery of lithium ions to the surface rather than bulk diffusion when particles are considered in nano dimensions [69, 70]. Therefore, the increase of specific surface area is advantageous for electrolyte penetration and fast lithium ion diffusion. Moreover, the presence of oxygen vacancies and $V^{4+}$ in MDLVO structure not only result in the formation of more open structure and possible nucleation centers for phase transformation during $Li^+$ insertion and extraction processes, but also improve the conductivity of cathode and consequently lead to the much higher capacity and rate performance of the MDLVO electrode.

## 4. Conclusions

Mo-doped $LiV_3O_8$ nanorod-assembled nanosheets were successfully synthesized

by a facile hydrothermal reaction followed with thermal annealing without any additives. The nanorods were found to form on the surface of MDLVO nanosheets after heat treatment. Raman band shifts to lower wavenumbers confirmed the occurrence of lattice distortion in MDLVO material, which proves that $Mo^{6+}$ substitutes $V^{5+}$ in $LiV_3O_8$ layer. This substitutional doping is considered to increase the stability of crystal structure during lithium ion insertion/extraction processes and be the reason of good cycling stability. The XPS results indicated that $V^{4+}$ and oxygen vacancies appeared in MDLVO material, which result in the formation of more open structure and high electronic conductivity of cathode material. The BET surface area of MDLVO (400) increased about 78% compared with pure $LiV_3O_8$ calcined at 400℃. The higher BET surface area is favorable for fast electrolyte penetration and lithium ion diffusion. The appropriate pore size distribution (the peak of pore size is 22.4 nm calculated by BJH method) in MDLVO (400) nanosheets can provide excellent channels and cavities for complete, homogeneous and easy $Li^+$ intercalation and diffusion. All of these lead to high capacity and rate capability of MDLVO (400). Therefore, MDLVO (400) nanorod-assembled nanosheets display significantly improved capacity and much better cycling stability and rate capability.

**Acknowledgments**

This work was supported by the "thousands talents" program for pioneer researcher and his innovation team, China. This work was also supported by the National Science Foundation of China (51374029), Program for New Century Excellent Talents in University (NCET-13-0668).

**References**

[1] J. Lee, A. Urban, X. Li, D. Su, G. Hautier, G. Ceder, Science 343 (2014) 519-522.

[2] B. Guo, X. Yu, X.G. Sun, M. Chi, Z.A. Qiao, J. Liu, Y.S. Hu, X.Q. Yang, J.B. Goodenough, S. Dai, Energy Environ. Sci. 7 (2014) 2220-2226.

[3] S.Y. Lee, K.H. Choi, W.S. Choi, Y.H. Kwon, H.R. Jung, H.C. Shin, J.Y. Kim, Energy Environ. Sci. 6 (2013) 2414-2423.

[4] D. Liu, G. Cao, Energy Environ. Sci. 3 (2010) 1218-1237.

[5] S.T. Myung, K. Amine, Y.K. Sun, J. Mater. Chem. 20 (2010) 7074-7095.

[6] Y.Q. Qiao, X.L. Wang, J.P. Zhou, J. Zhang, C.D. Gu, J.P. Tu, J. Power Sources 198 (2012) 287-293.

[7] S. Huang, J.P. Tu, X.M. Jian, Y. Lu, S.J. Shi, X.Y. Zhao, T.Q. Wang, X.L. Wang, C.D. Gu, J. Power Sources 245 (2014) 698-705.

[8] R. Mo, Y. Du, N. Zhang, D. Rooney, K. Sun, Chem. Commun. 49 (2013) 9143-9145.

[9] L.A. Depicciotto, K.T. Adendorff, D.C. Liles, M.M. Thackeray, Solid State Ionics 62 (1993) 297-307.

[10] A.D. Wadsley, Acta Crystallogr. 10 (1957) 261-267.

[11] J. Kawakita, T. Miura, T. Kishi, Solid State Ionics 118 (1999) 141-147.

[12] Y. Mizuno, E. Hosono, T. Saito, M. Okubo, D. Nishio-Hamane, K. Oh-ishi, T. Kudo, H. Zhou, J. Phys. Chem. C 116 (2012) 10774-10780.

[13] J. Proell, H. Kim, A. Pique, H.J. Seifert, W. Pfleging, J. Power Sources 255 (2014) 116-124.

[14] Y. Zhao, L. Peng, B. Liu, G. Yu, Nano Lett. 14 (2014) 2849-2853.

[15] R. Ramaraghavulu, K. Sivaiah, S. Buddhudu, Fer 432 (2012) 55-64.

[16] M. Onoda, J. Phys.: Condens. Matter 16 (2004) 8957-8969.

[17] S. Sarkar, H. Banda, S. Mitra, Electrochim. Acta 99 (2013) 242-252.

[18] D. Sun, G. Jin, H. Wang, X. Huang, Y. Ren, J. Jiang, H. He, Y. Tang, J. Mater. Chem. A 2 (2014) 8009-8016.

[19] X. Ren, S. Hu, C. Shi, P. Zhang, Q. Yuan, J. Liu, J. Solid State Electrochem. 16 (2012) 2135-2141.

[20] H. Wang, Y. Ren, Y. Wang, W. Wang, S. Liu, CrystEngComm 14 (2012) 2831-2836.

[21] Y. Feng, Y. Li, F. Hou, J. Power Sources 187 (2009) 224-228.

[22] A. Pan, J. Liu, J.G. Zhang, G. Cao, W. Xu, Z. Nie, X. Jie, D. Choi, B.W. Arey, C. Wang, S. Liang, J. Mater. Chem. 21 (2011) 1153-1161.

[23] P. Mei, X.L. Wu, H. Xie, L. Sun, Y. Zeng, J. Zhang, L. Tai, X. Guo, L. Cong, S. Ma, C. Yao, R. Wang, RSC Adv. 4 (2014) 25494-25501.

[24] S. Huang, Y. Lu, T.Q. Wang, C.D. Gu, X.L. Wang, J.P. Tu, J. Power Sources 235 (2013) 256-264.

[25] P. Samarasingha, D.H. Tran-Nguyen, M. Behm and A. Wijayasinghe, Electrochim. Acta, 53 (2008) 7995-8000.

[26] A. Wijayasinghe, B. Bergman and C. Lagergren, Solid State Ionics, 177 (2006) 165-173.

[27] D. Wang, L. Cao, J. Huang, J. Wu, Ceram. Int. 38 (2012) 2647-2652.

[28] H. Liu, Y. Wang, K. Wang, Y. Wang, H. Zhou, J. Power Sources 192 (2009) 668-673.

[29] J. Liu, W. Liu, Y. Wan, S. Ji, J. Wang, Y. Zhou, RSC Adv. 2 (2012) 10470-10474.

[30] H. Liu, Y. Wang, W. Yang, H. Zhou, Electrochim. Acta 56 (2011) 1392-1398.

[31] X. Zhang, R. Frech, Electrochim. Acta 43 (1998) 861-868.

[32] A. Pan, J.G. Zhang, G. Cao, S. Liang, C. Wang, Z. Nie, B.W. Arey, W. Xu, D. Liu, J. Xiao, G. Li, J. Liu, J. Mater. Chem. 21 (2011) 10077-10084.

[33] F. Haass, A.H. Adams, T. Buhrmester, G. Schimanke, M. Martin, H. Fuess, PCCP 5 (2003) 4317-4324.

[34] G. Yang, G. Wang, W.H. Hou, J. Phys. Chem. B 109 (2005) 11186-11196.

[35] L. Si, Z. Yuan, J. Liang, L. Hu, Y. Zhu, Y. Qian, J. Mater. Chem. A 2 (2014) 9784-9791.

[36] P. Qin, G. Fang, W. Ke, F. Cheng, Q. Zheng, J. Wan, H. Lei, X. Zhao, J. Mater. Chem. A 2 (2014) 2742-2756.

[37] G.A. Sawatzky, D. Post, PhRvB 20 (1979) 1546-1555.

[38] Y. Zhang, P. Xiao, X. Zhou, D. Liu, B.B. Garcia, G. Cao, J. Mater. Chem. 19

(2009) 948-953.

[39] Y. Li, J. Yao, E. Uchaker, M. Zhang, J. Tian, X. Liu, G. Cao, J. Phys. Chem. C 117 (2013) 23507-23514.

[40] P. Gomez-Romero, Adv. Mater. 13 (2001) 163-174.

[41] I. Boyano, M. Bengoechea, I. de Meatza, O. Miguel, I. Cantero, E. Ochoteco, J. Rodriguez, M. Lira-Cantu, P. Gomez-Romero, J. Power Sources 166 (2007) 471-477.

[42] J. Zhu, L. Cao, Y. Wu, Y. Gong, Z. Liu, H.E. Hoster, Y. Zhang, S. Zhang, S. Yang, Q. Yan, P.M. Ajayan, R. Vajtai, Nano Lett. 13 (2013) 5408-5413.

[43] Y. Li, J. Yao, E. Uchaker, J. Yang, Y. Huang, M. Zhang, G. Cao, Adv. Eng. Mater. 3 (2013) 1171-1175.

[44] V. Petkov, P.N. Trikalitis, E.S. Bozin, S.J.L. Billinge, T. Vogt, M.G. Kanatzidis, J. Am. Chem. Soc. 124 (2002) 10157-10162.

[45] J. Livage, Chem. Mater. 3 (1991) 578-593.

[46] J.G. Xie, J.X. Li, H. Zhan, Y.H. Zhou, Mater. Lett. 57 (2003) 2682-2687.

[47] X. Xu, Y.Z. Luo, L.Q. Mai, Y.L. Zhao, Q.Y. An, L. Xu, F. Hu, L. Zhang, Q.J. Zhang, Npg Asia Mater. 4 (2012).

[48] J. Kawakita, Y. Katayama, T. Miura, T. Kishi, Solid State Ionics 107 (1998) 145-152.

[49] J. Kawakita, T. Miura, T. Kishi, J. Power Sources 83 (1999) 79-83.

[50] J. Kawakita, M. Majima, T. Miura, T. Kishi, J. Power Sources 66 (1997) 135-139.

[51] S. Caes, J.C. Arrebola, N. Krins, P. Eloy, E.M. Gaigneaux, C. Henrist, R. Cloots, B. Vertruyen, J. Mater. Chem. A 2 (2014) 5809-5815.

[52] M. Zhao, L.F. Jiao, H.T. Yuan, Y. Feng, M. Zhang, Solid State Ionics 178 (2007) 387-391.

[53] Z.J. Wu, Y. Zhou, J. Power Sources 199 (2012) 300-307.

[54] J. Su, X.L. Wu, J.S. Lee, J. Kim and Y.G. Guo, J. Mater. Chem. A 1 (2013) 2508-2514.

[55] A. Sakunthala, M.V. Reddy, S. Selvasekarapandian, B.V.R. Chowdari, P.C. Selvin, J. Phys. Chem. C 114 (2010) 8099-8107.

[56] S. Jouanneau, A. Verbaere, S. Lascaud, D. Guyomard, Solid State Ionics 177

(2006) 311-315.

[57] S.H. Ju, Y.C. Kang, Electrochim. Acta 55 (2010) 6088-6092.

[58] D. Wang, L. Cao, J. Huang, J. Wu, Ceram. Int. 39 (2013) 3759-3764.

[59] Y. Wang, X. Xu, C. Cao, C. Shi, W. Mo, H. Zhu, J. Power Sources 242 (2013) 230-235.

[60] H. Guo, L. Liu, H. Shu, X. Yang, Z. Yang, M. Zhou, J. Tan, Z. Yan, H. Hu, X. Wang, J. Power Sources 247 (2014) 117-126.

[61] S. Jouanneau, A.L. La Salle, A. Verbaere, M. Deschamps, S. Lascaud, D. Guyomard, J. Mater. Chem. 13 (2003) 921-927.

[62] S. Jouanneau, A.L. La Salle, A. Verbaere, D. Guyomard, J. Electrochem. Soc. 152 (2005) A1660-A1667.

[63] D. Liu, Y. Liu, A. Pan, K.P. Nagle, G.T. Seidler, Y.H. Jeong, G. Cao, J. Phys. Chem. C 115 (2011) 4959-4965.

[64] Y. Gao, J. Ma, X. Wang, X. Lu, Y. Bai, Z. Wang, L. Chen, J. Mater. Chem. A 2 (2014) 4811-4818.

[65] H. Wang, K. Huang, Y. Ren, X. Huang, S. Liu, W. Wang, J. Power Sources 196 (2011) 9786-9791.

[66] Y.J. Kang, J.H. Kim, S.W. Lee, Y.K. Sun, Electrochim. Acta 50 (2005) 4784-4791.

[67] H. Wang, W. Wang, Y. Ren, K. Huang, S. Liu, J. Power Sources 199 (2012) 263-269.

[68] R. Mo, Y. Du, N. Zhang, D. Rooney, K. Sun, J. Power Sources 257 (2014) 319-324.

[69] B. Kang, G. Ceder, Nature 458 (2009) 190-193.

[70] Q. Shi, J. Liu, R. Hu, M. Zeng, M. Dai, M. Zhu, RSC Adv. 2 (2012) 7273-7278.

**Figure captions:**

Figure 1 Schematic illustration of the synthesis route of Mo-doped $LiV_3O_8$ nanorod-assembled nanosheets in this work.

Figure 2 TGA and DTA results for Mo-doped $LiV_3O_8$ cryogel.

Figure 3 XRD patterns of $LiV_3O_8$ calcined at 400℃ and Mo-doped $LiV_3O_8$ (MDLVO) calcined at different temperatures.

Figure 4 Raman spectra of pure $LiV_3O_8$ and Mo-doped $LiV_3O_8$ (MDLVO) nanorod-assembled nanosheets calcined at 400℃.

Figure 5 XPS spectra of Mo-doped $LiV_3O_8$ calcined at 400℃: (a) survey spectrum and high-solution (b) Mo 3d, (c) V 2p spectra.

Figure 6 FE-SEM (a, b), TEM (c, d) and SEM images of Mo-doped $LiV_3O_8$ (400) and its corresponding EDS maps of Li, Mo, V and O elements (e).

Figure 7 $N_2$ adsorption/desorption isotherm and the SEM image (inset) of $LiV_3O_8$ nanosheets calcined at 400℃ (a), $N_2$ adsorption/desorption isotherm and the corresponding BJH pore-size distribution curves (inset) of Mo doped $LiV_3O_8$ nanosheets calcined at 400℃ (b).

Figure 8 The second-cycle CV curves for pure $LiV_3O_8$ calcined at 400℃ and Mo-doped $LiV_3O_8$ (400) electrodes at a scan rate of 0.1 mV $s^{-1}$ over the range of 2.0-4.0 V (*vs*. $Li/Li^+$).

Figure 9 Discharge/charge curves (a) and cyclic performance (b) of pure $LiV_3O_8$ and Mo-doped $LiV_3O_8$ calcined at 400℃ at a current density of 300 mA $g^{-1}$.

Figure 10 (a) Discharge capacities of pure $LiV_3O_8$ calcined at 400℃ and Mo-doped $LiV_3O_8$ (400) electrodes at various current densities and (b) discharge/charge curves of Mo-doped $LiV_3O_8$ (400) electrode at various current densities.

Figure 11 (a) Nyquist plots of $LiV_3O_8$ calcined at 400℃ and Mo-doped $LiV_3O_8$ (400) electrodes at 2.7 V and (b) the relationship curves between $Z'$ and $\omega^{-1/2}$ in the low frequency range.

Figure 12 Cyclic stabilities of Mo-doped $LiV_3O_8$ electrodes calcined at different temperatures at a current density of 300 mA $g^{-1}$.

# Mo-doped $LiV_3O_8$ nanorod-assembled nanosheets as a high performance cathode material for lithium ion batteries

Huanqiao Song[a, *], Yaguang Liu[a], Cuiping Zhang[a], Chaofeng Liu[a] and Guozhong Cao[a, b, *]

[a]*Beijing Institute of Nanoenergy and Nanosystems, Chinese Academy of Sciences, Beijing 100083, China.*

[b]*Department of Materials and Engineering, University of Washington, Seattle, WA 98195-2120, USA*

## Graphical Abstract

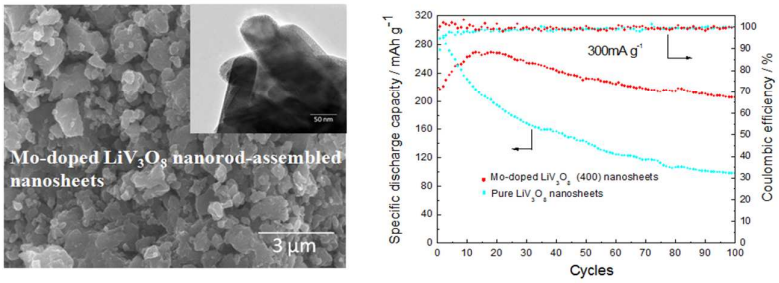


A new Mo-doped $LiV_3O_8$ (MDLVO) nanorod-assembled nanosheet material was prepared by a simple hydrothermal reaction followed with thermal annealing. This nanosheet material demonstrated a maximum discharge capacity of 269 mAh $g^{-1}$ at a current density of 300 mA $g^{-1}$ in the voltage range of 4.0 to 2.0 V and excellent rate and cycle performance as a cathode material for LIBs. The formation mechanism of MDLVO nanorod-assembled nanosheets and the correlations between the excellent electrochemical performance and the microstructure of MDLVO nanosheets are analyzed and elucidated.

* Corresponding author at: Beijing Institute of Nanoenergy and Nanosystems, Chinese Academy of Sciences, Beijing 100083, China.
E-mail: songhuanqiao@binn.cas.cn; gzcao@u.washington.edu.

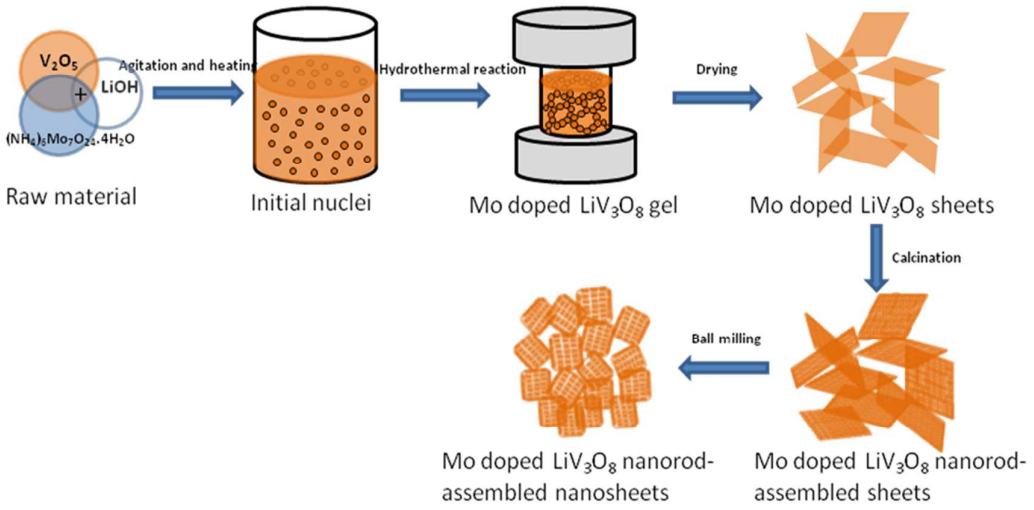


Figure 1 Schematic illustration of the synthesis route of Mo-doped $LiV_3O_8$ nanorod-assembled nanosheets in this work.

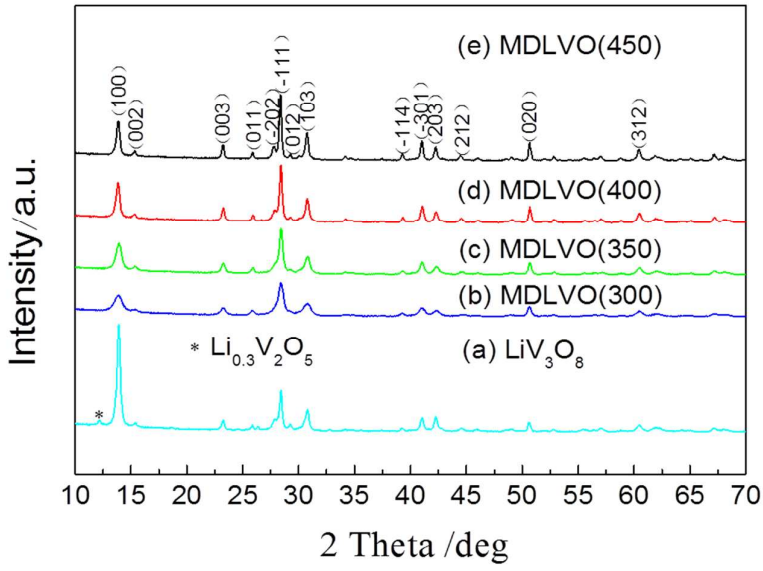


Figure 3 XRD patterns of $LiV_3O_8$ calcined at 400℃ and Mo-doped $LiV_3O_8$ (MDLVO) calcined at different temperatures.

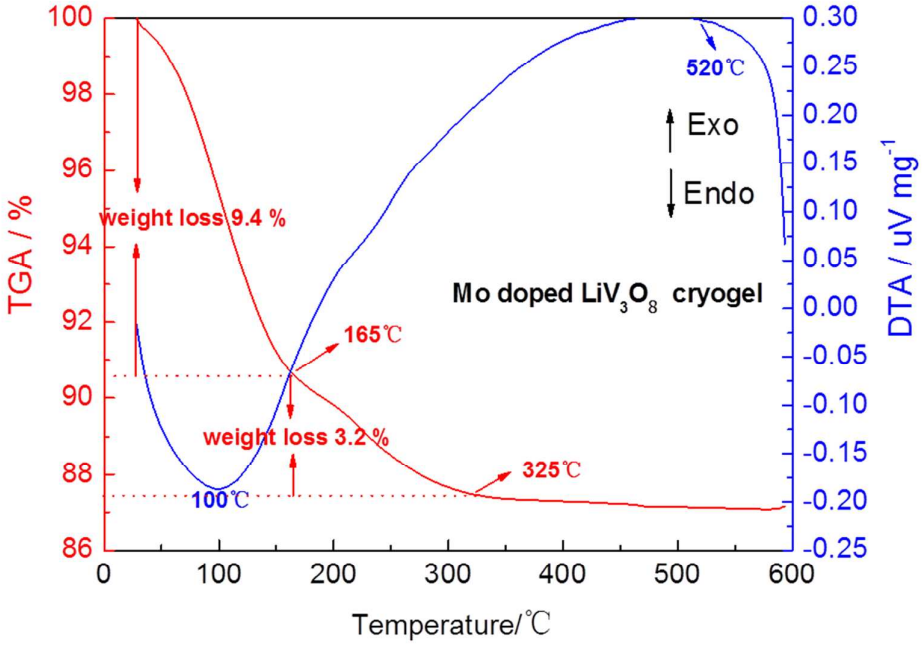


Figure 2 TGA and DTA results for Mo-doped $LiV_3O_8$ cryogel.

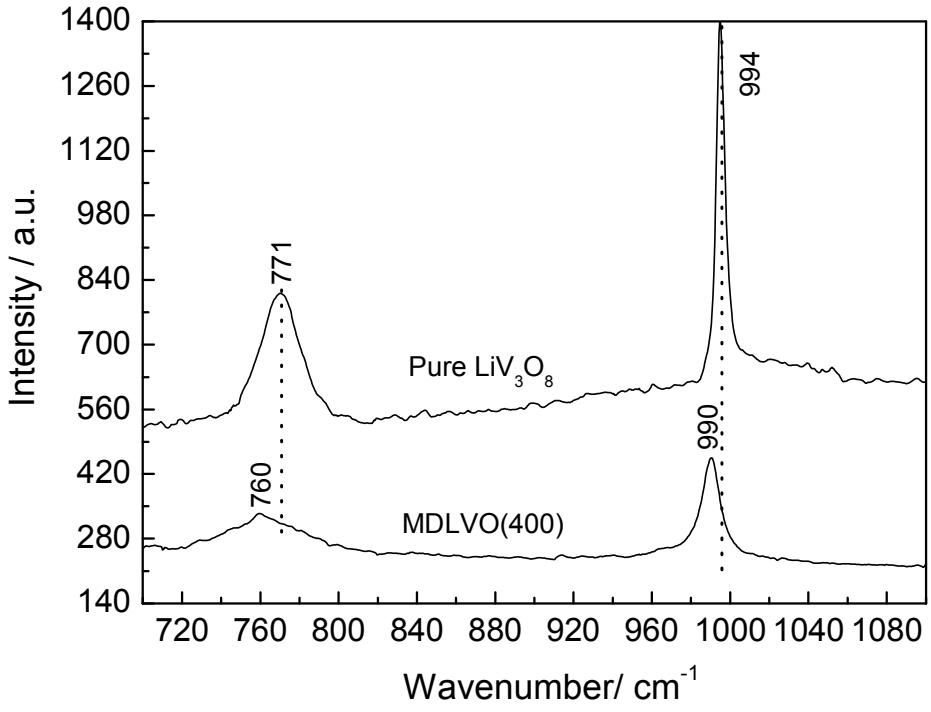


Figure 4 Raman spectra of pure $LiV_3O_8$ and Mo-doped $LiV_3O_8$ (MDLVO) nanorod-assembled nanosheets calcined at 400℃.

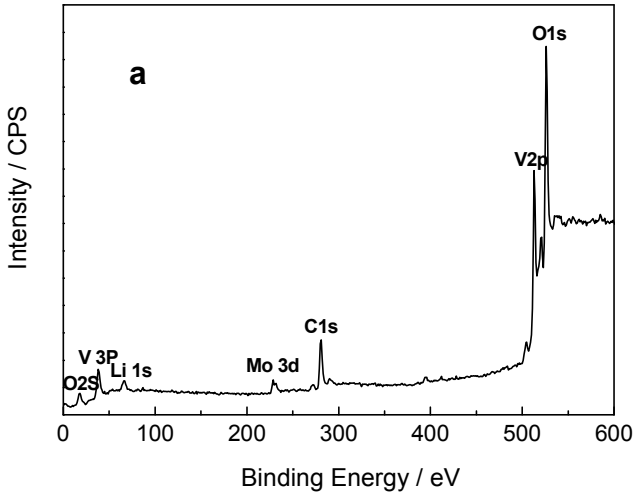


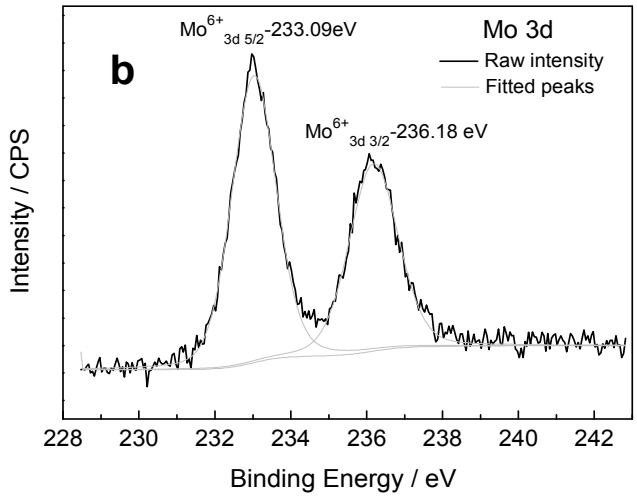

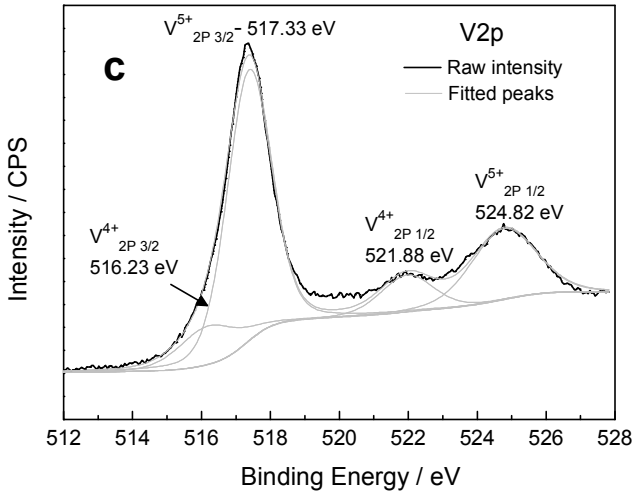


Figure 5 XPS spectra of Mo-doped $LiV_3O_8$ calcined at 400℃: (a) survey spectrum and high-solution (b) Mo 3d, (c) V 2p spectra.

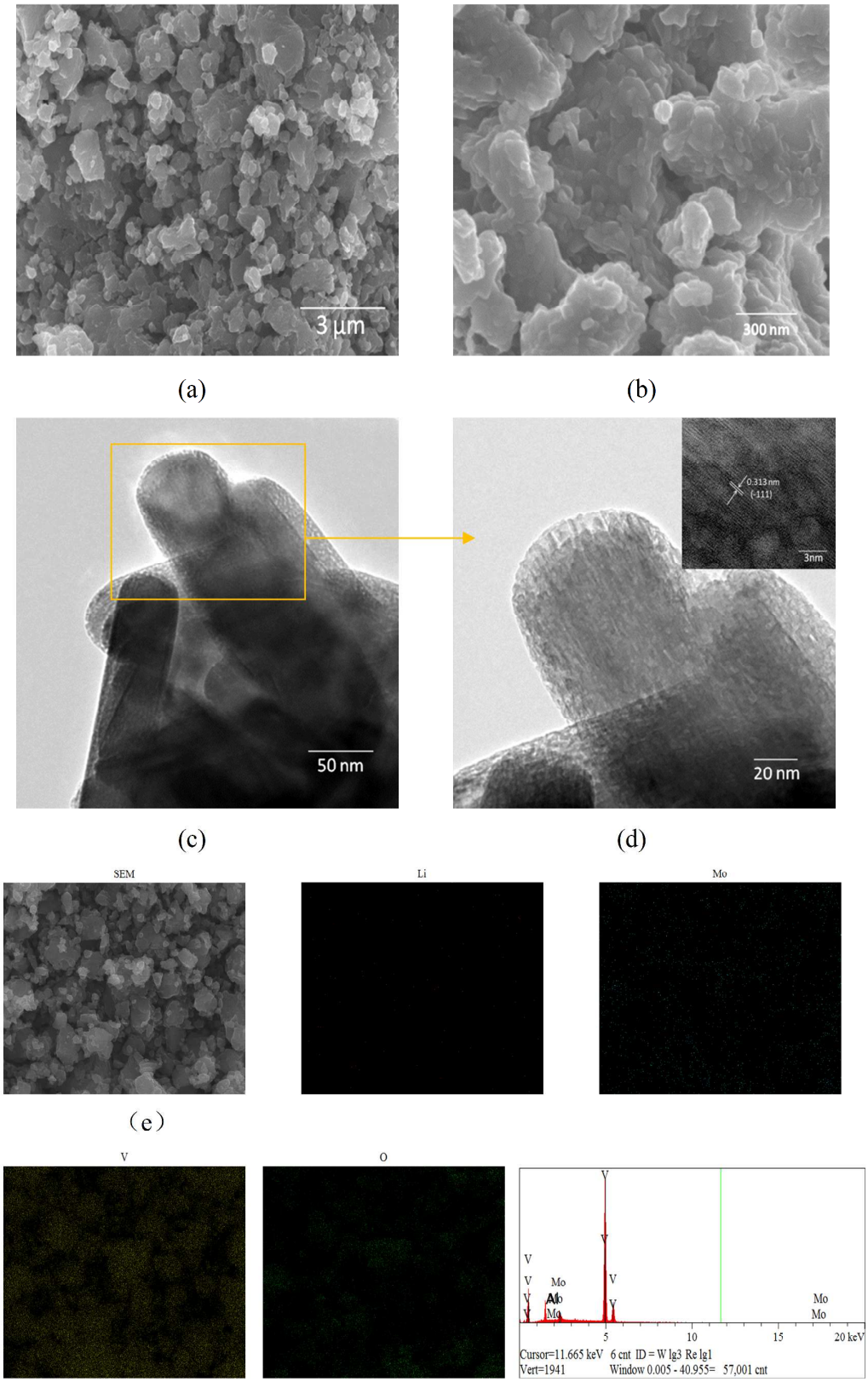


Figure 6 FE-SEM (a, b), TEM (c, d) and SEM images of Mo-doped $LiV_3O_8$ (400) and its corresponding EDS maps of Li, Mo, V and O elements (e).

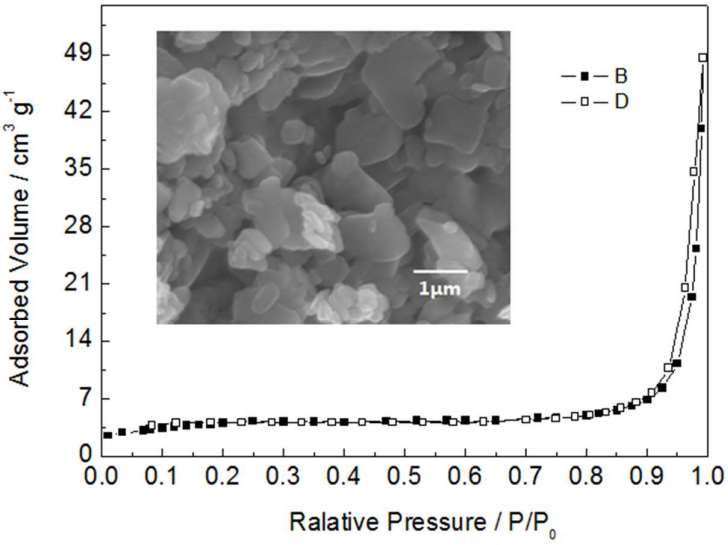


(a)

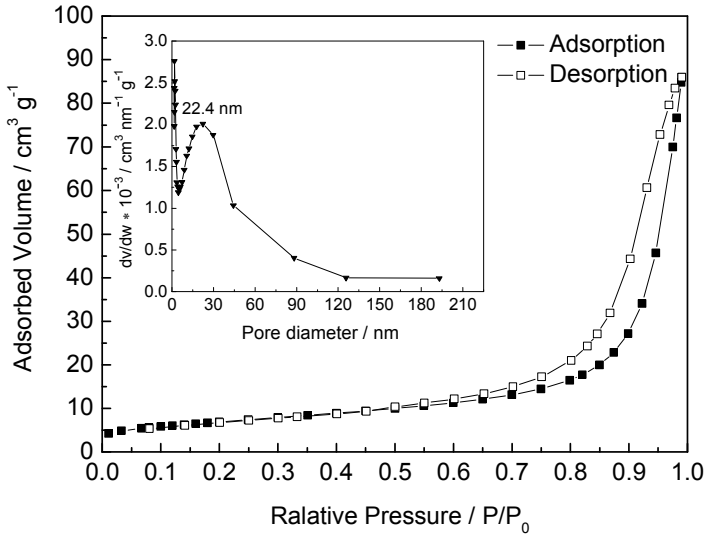


(b)

Figure 7 $N_2$ adsorption/desorption isotherm and the SEM image (inset) of $LiV_3O_8$ nanosheets calcined at 400℃ (a), $N_2$ adsorption/desorption isotherm and the corresponding BJH pore-size distribution curves (inset) of Mo doped $LiV_3O_8$ nanosheets calcined at 400℃ (b).

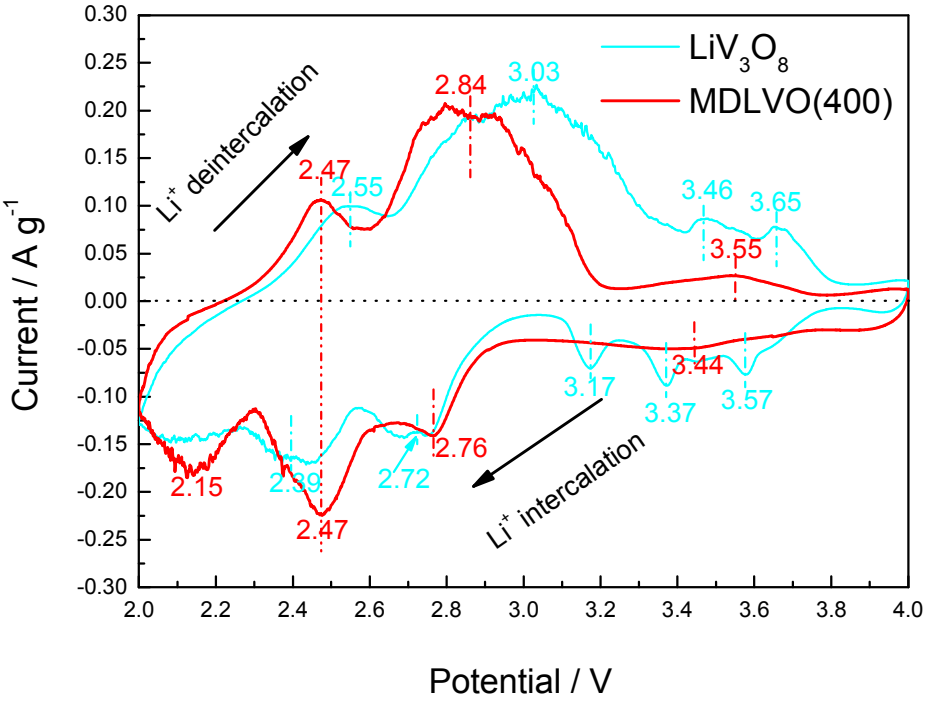


Figure 8 The second-cycle CV curves for pure $LiV_3O_8$ calcined at 400℃ and Mo-doped $LiV_3O_8$ (400) electrodes at a scan rate of 0.1 mV $s^{-1}$ over the range of 2.0-4.0 V (*vs*. $Li/Li^+$).

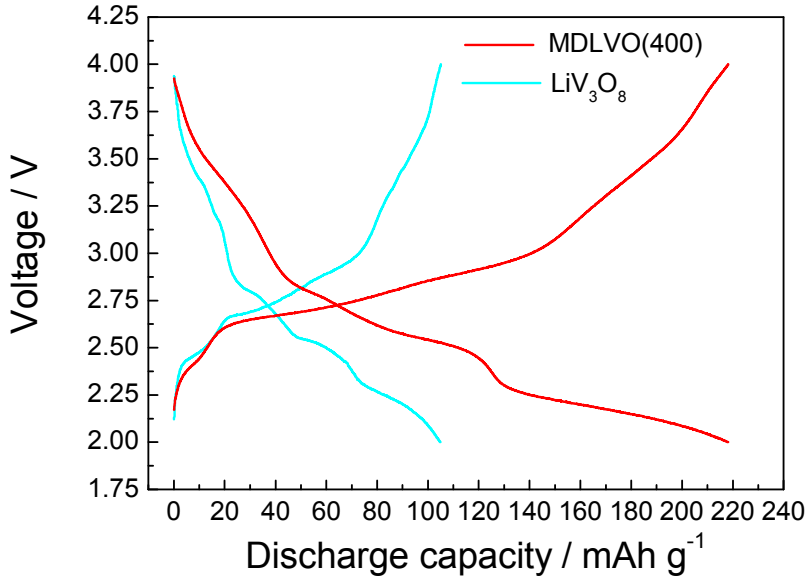


(a)

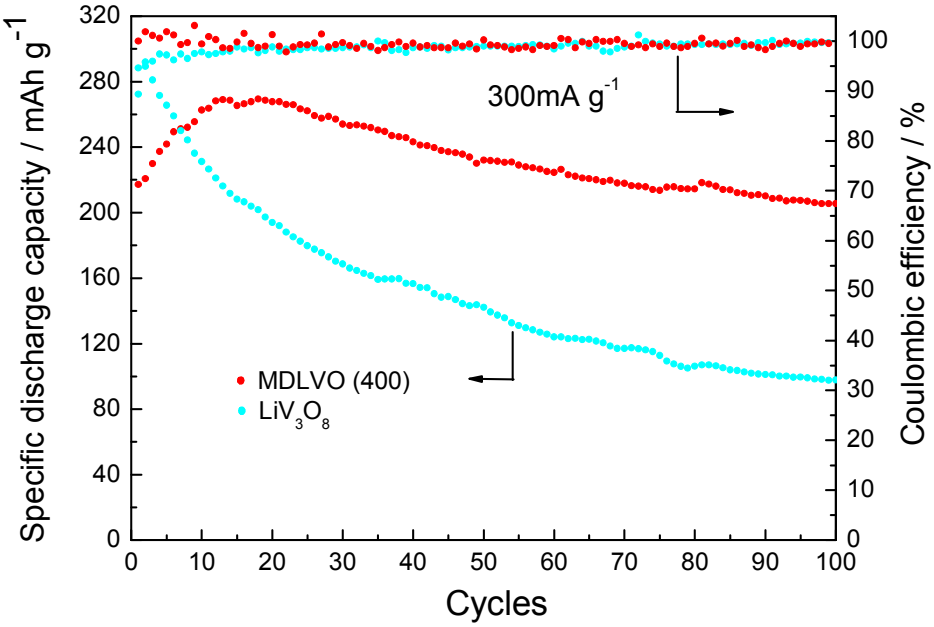


(b)

Figure 9 Discharge/charge curves (a) and cyclic performance (b) of pure $LiV_3O_8$ and Mo-doped $LiV_3O_8$ calcined at 400℃ at a current density of 300 mA $g^{-1}$.

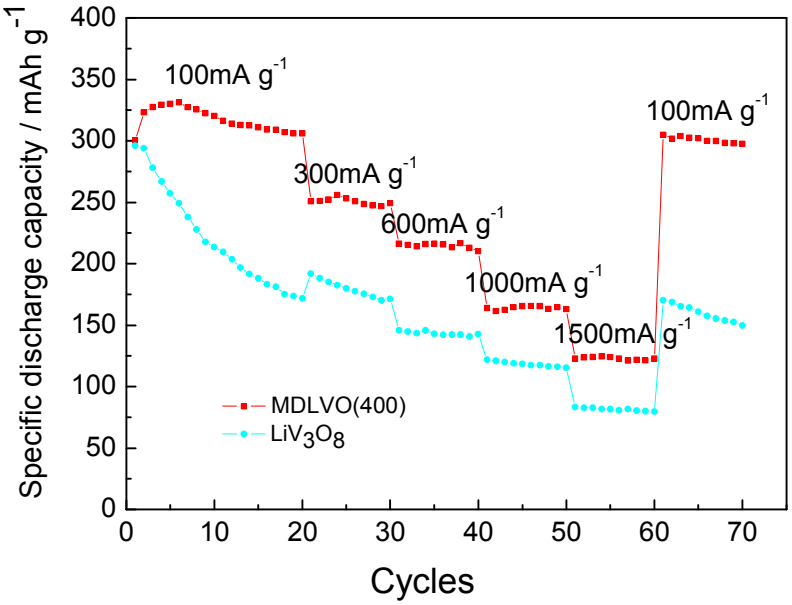


(a)

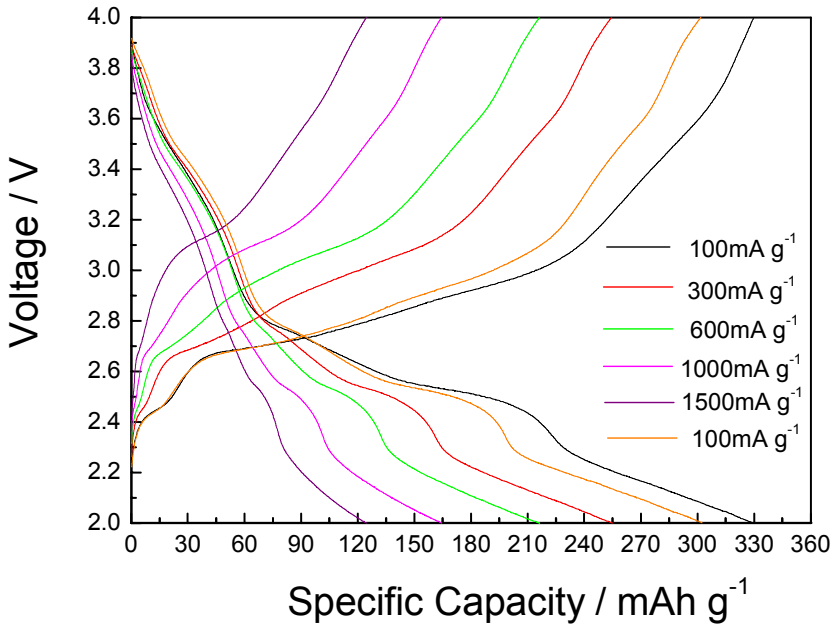


(b)

Figure 10 (a) Discharge capacities of pure $LiV_3O_8$ calcined at 400℃ and Mo-doped $LiV_3O_8$ (400) electrodes at various current densities and (b) discharge/charge curves of Mo-doped $LiV_3O_8$ (400) electrode at various current densities.

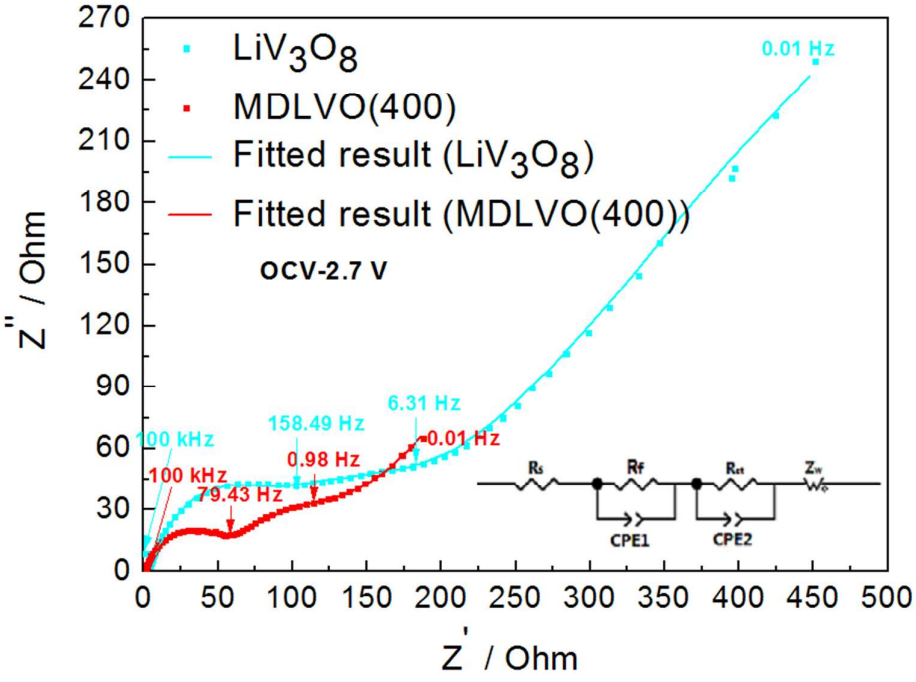


(a)

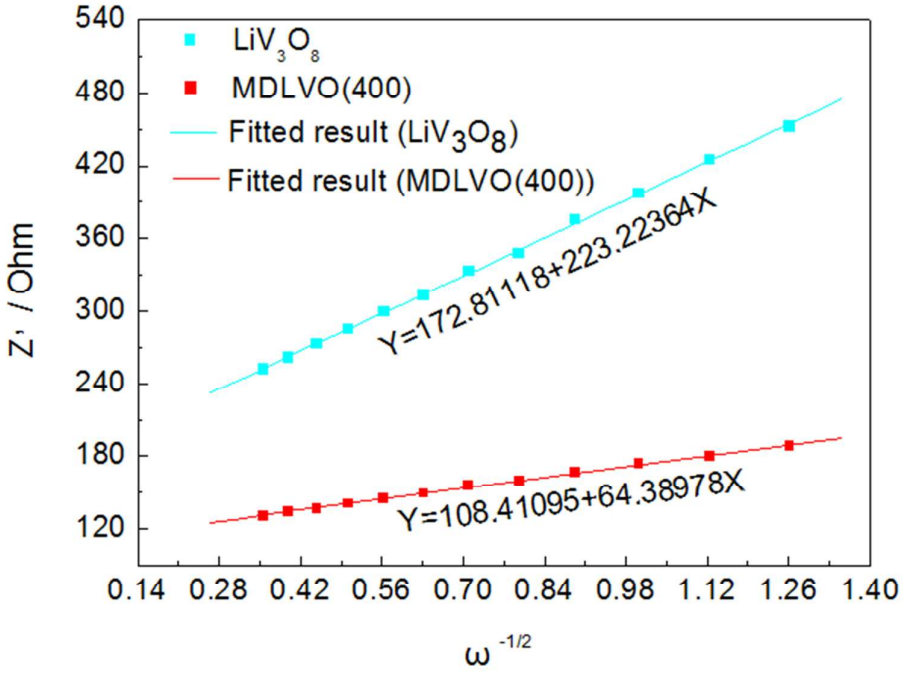


(b)

Figure 11 (a) Nyquist plots of $LiV_3O_8$ calcined at 400℃ and Mo-doped $LiV_3O_8$ (400) electrodes at 2.7 V and (b) the relationship curves between $Z'$ and $\omega^{-1/2}$ in the low frequency range.

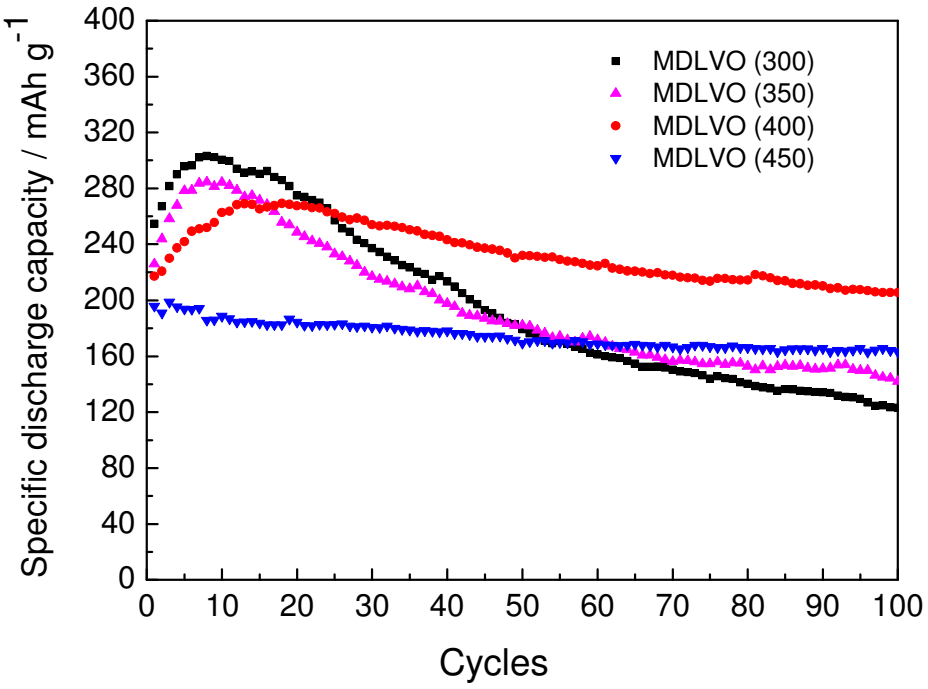


Figure 12 Cyclic stabilities of Mo-doped $LiV_3O_8$ electrodes calcined at different temperatures at a current density of 300 mA $g^{-1}$.